npj Computational Materials

www.nature.com/npjcompumats

ARTICLE OPEN

Check for updates

Efficient electron extraction of SnO_2 electron transport layer for lead halide perovskite solar cell

Junu Kim[1], Kwang S. Kim[1,2]✉ and Chang Woo Myung[2]✉

SnO_2 electron transport layer (ETL) has been spotlighted with its excellent electron extraction and stability over TiO_2 ETL for perovskite solar cells (PSCs), rapidly approaching the highest power conversion efficiency. Thus, how to boost the performance of ETL is of utmost importance and of urgent need in developing more efficient PSCs. Here we elucidate the atomistic origin of efficient electron extraction and long stability of SnO_2-based PSCs through the analysis of band alignment, carrier injection, and interfacial defects in the $SnO_2/MAPbI_3$($MA = CH_3NH_3^+$) interface using unprecedentedly high level of first-principles calculations at the PBE0 + spin-orbit-coupling + dispersion-correction level for all possible terminations and MA directions. We find that Sn-*s* orbital plays a crucial role in carrier injection and defect tolerance. $SnO_2/MAPbI_3$ shows favorable conduction band alignments at both MAI- and PbI_2-terminations, which makes the solar cell performance of $SnO_2/MAPbI_3$ excel that of $TiO_2/MAPbI_3$. Different electron transfer mechanisms of dipole interaction and orbital hybridization at the MAI- and PbI_2-terminations indicate that post-transition metal (*sp* valence) oxide ETLs would outperform transition metal (*d* valence) oxide ETLs for PSCs.

npj Computational Materials (2020)6:100; https://doi.org/10.1038/s41524-020-00370-y

INTRODUCTION

Recently, lead halide perovskite (LHP) solar cells (PSCs) based on ABX_3 [$A = Cs^+$, $CH_3NH_3^+$ (MA^+), $CHN_2H_4^+$ (FA^+), $B = Pb^{2+}$, Sn^{2+}, Ge^{2+}, $X = I^-$, Br^-, Cl^-] have become one of the most promising large-scale photovoltaic materials by achieving the power conversion efficiency over 25%[1–7]. The electron transport layer (ETL) plays a crucial role in extracting and transporting photo-generated electron carriers and serves as a hole-blocking layer by suppressing charge recombination as one of the most important components for photovoltaic devices[8]. The physical properties of the ETL, including charge mobility, energy level alignment, defect states, morphology, and related interfacial properties, are significant for the photovoltaic performance[9]. Until now, TiO_2 has been widely used as the ETL material for organic/inorganic PSCs[10,11]. However, TiO_2 shows some limitations as a stable and efficient ETL for PSCs[12–16,20]. The conduction band minimum (CBM) of TiO_2 is slightly higher than that of $MAPbI_3$[17], which hinders the electron extraction from ETL[20]. TiO_2 decomposes under the exposure to ultraviolet (UV) for a long time, which is not suitable for commercialization of PSCs[12–14]. High temperature annealing for processing TiO_2 also hampers elaborate device fabrication[15]. Defect trap states such as oxygen vacancy in TiO_2 increases non-radiative loss and degrade the device performance[16].

Many experimental efforts have been paid to overcome the limitations of TiO_2 and to find novel ETL materials, including SnO_2[18], La-doped $BaSnO_3$[19], and ZnO[20]. Among many candidates, SnO_2 has shown an excellent chemical stability, UV-resistance, superior band alignment, high charge extraction, and less photocatalytic activity compared with TiO_2 or other ETLs[21–26,28,29]. SnO_2 has shown a favorable CBM alignment to LHP, allowing minimum loss of open-circuit voltage[21]. UV spectroscopy and femtosecond transient absorption measurement showed that SnO_2 exhibits the better electron extraction than TiO_2[21]. Since SnO_2 has a large band gap (E_g)[22] ~3.6 eV (vs. $E_g(TiO_2)$ ~3.0 eV)[23], most of visible lights pass through SnO_2[24]. SnO_2 prohibits absorption of UV because of the large E_g, protecting from UV exposure[25,26]. In addition, the bulk electron mobility in SnO_2 is two orders of magnitude higher than that of TiO_2[27]. SnO_2 is easily processed at low-temperature, which is suitable for large-scale commercialization[28,29].

Although SnO_2 has been used as an alternative ETL for PSCs till now, the electron extraction mechanism of SnO_2-based PSCs has not been studied yet. Here, we show a comparative study of rutile $SnO_2/MAPbI_3$ and rutile $TiO_2/MAPbI_3$ interfaces to uncover the mechanism behind the superior SnO_2-based PSCs by employing first-principles calculations at the hybrid Perdew–Burke–Ernzerhof (PBE0) + spin-orbit-coupling (SOC) + Tkatchenko–Scheffler (TS) dispersion correction (PBE0-SOC-TS) level. Because the electronic structure of the interface is largely affected by the termination type and the alignment of organic A-site cation MA[1], we investigate various directions of MA ([001], [011], and [111]) and termination types for $MAPbI_3$ (MAI- and PbI_2-terminations) at the $SnO_2/MAPbI_3$ and $TiO_2/MAPbI_3$ interfaces. The $SnO_2/MAPbI_3$ shows superior features to $TiO_2/MAPbI_3$, including CBM band alignments, large electron carrier injection, and the suppression of mid-gap defect states. In addition, we discuss a fundamental difference in electron extraction mechanisms between MAI-terminated (dipole polarization) and PbI_2-terminated (orbital hybridization) $MAPbI_3$.

RESULTS AND DISCUSSION

We employ $\sqrt{2} \times \sqrt{2}$ supercell of (001) plane rutile SnO_2, rutile TiO_2, and unit cell of (001) plane cubic $MAPbI_3$ surfaces for the study. The slab consists of symmetric SnO_2 or TiO_2 (5 layers, 22 Sn/Ti atoms and 44 O atoms) and $MAPbI_3$ (001) (3 layers, MAI-termination: 4 MA molecules, 3 Pb atoms, and 10 I atoms,

[1]Center for Superfunctional Materials, Department of Physics, School of Natural Science, Ulsan National Institute of Science and Technology (UNIST), Ulsan 44919, Korea. [2]Center for Superfunctional Materials, Department of Chemistry, School of Natural Science, Ulsan National Institute of Science and Technology (UNIST), Ulsan 44919, Korea. ✉email: kimks@unist.ac.kr; cwmyung@unist.ac.kr

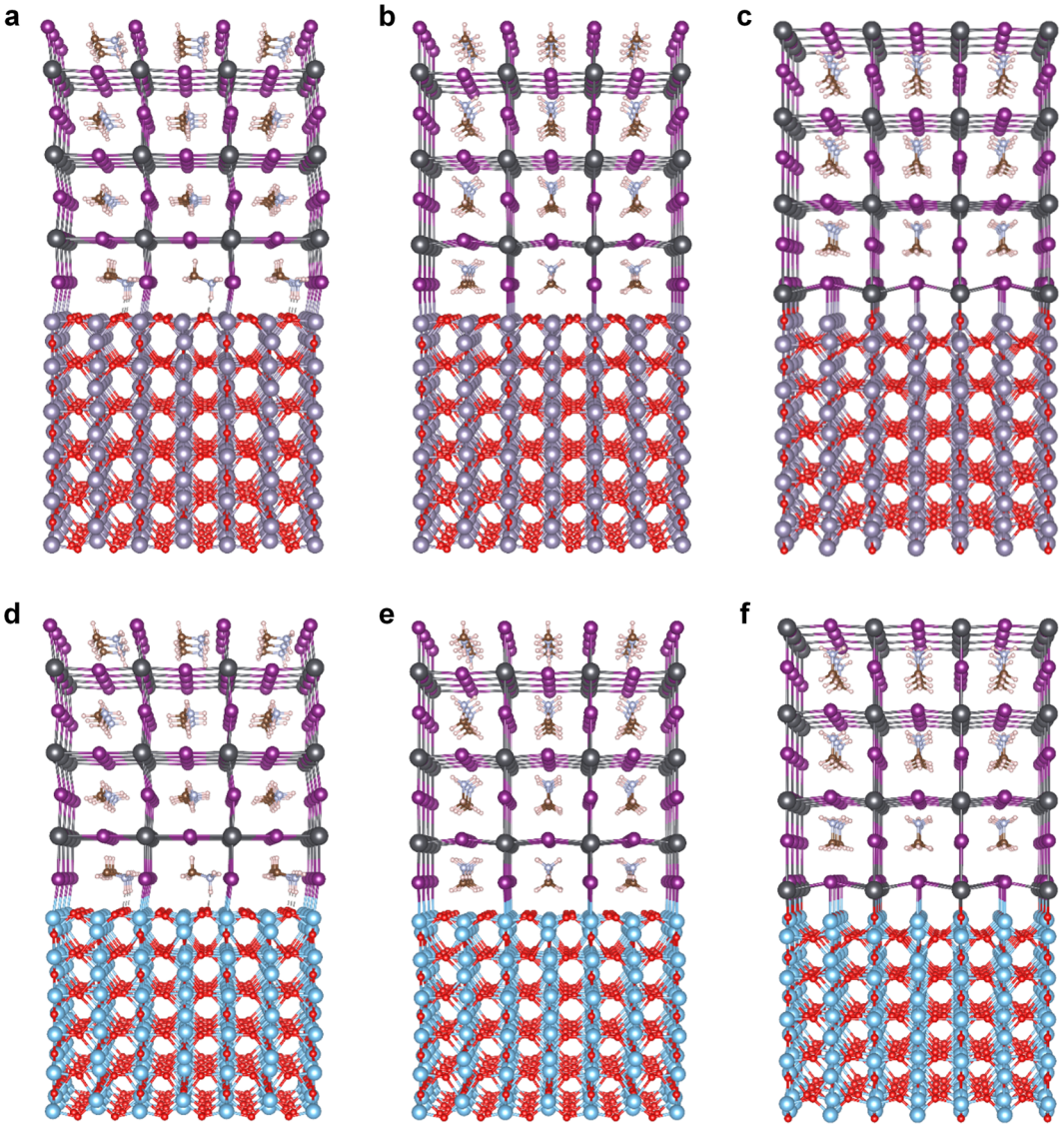

Fig. 1 Optimized geometry of SnO_2/$MAPbI_3$ and TiO_2/$MAPbI_3$ interfaces. SnO_2/$MAPbI_3$ interfaces of **a** MAI-termination with the SSHB, **b** MAI-termination without the SSHB, and **c** PbI_2-termination. TiO_2/$MAPbI_3$ interfaces of **d** MAI-termination with the SSHB, **e** MAI-termination without the SSHB, and **f** PbI_2-termination [Pb (black), I (purple), C (brown), N (light blue), H (white), Sn (dark blue), Ti (blue), and O (red)]. Dotted gray line between H and O at the interface represents the short strong hydrogen bonding (SSHB).

PbI_2-termination: 3 MA molecules, 4 Pb atoms, and 11 I atoms), where the lattice mismatches between $MAPbI_3$ and SnO_2 or TiO_2 are as small as ~3% with a vacuum size of ~40 Å. Considering the lattice parameter of pristine SnO_2 ($\sqrt{2}\times\sqrt{2}$ supercell) and $MAPbI_3$ is about 6.7 and 6.3 Å, respectively, we choose the average lattice parameter of 6.5 Å which makes the lattice mismatch of both sides being 3%. With combinations of MAI- and PbI_2-terminations with [001], [011], and [111] directions of MA in $MAPbI_3$, six types of SnO_2/$MAPbI_3$ (Fig. 1a–c, Supplementary Figs. 1 and 2) and TiO_2/$MAPbI_3$ (Fig. 1d–f, Supplementary Figs. 3 and 4) interfaces are investigated. We mainly focused on the SnO_2/$MAPbI_3$ (Fig. 1a) and TiO_2/$MAPbI_3$ (Fig. 1d) interfaces with the [111] MA direction where the short strong hydrogen bonding (SSHB) exists after the geometry optimization being the lowest energy configuration[1]. Because the PbI_2-terminated SnO_2/$MAPbI_3$ has stronger binding energy along the [001] MA direction than either [011] or [111] (Supplementary Table 1), we focus on SnO_2/$MAPbI_3$ (Fig. 1c) and TiO_2/$MAPbI_3$ (Fig. 1f) interfaces with the [001] MA direction. Before the relaxation, each interface with [001], [011], and [111] MA orientation does not contain the SSHB. However, in the case of interface with [111] MA orientation, the MA molecule at the interface rotates during the relaxation so that the SSHB forms between the nitrogen atom of MA molecule and the oxygen atom of interfacial SnO_2. In contrast, in the case of interface with [001] and [011] MA orientation, MA molecules at the interface cannot rotate enough to form the SSHB during the relaxation. Supplementary Figs. 1 and 2 are the SnO_2/$MAPbI_3$ and TiO_2/$MAPbI_3$ interfaces before the relaxation, all of which do not contain the SSHB. Supplementary Figs. 3 and 4 are SnO_2/$MAPbI_3$ and TiO_2/$MAPbI_3$ interface after the relaxation and only Supplementary Figs. 3c and 4c contain the SSHB.

We note that the interfacial binding energy at the SnO_2/$MAPbI_3$ interface (Fig. 1a–c) is larger than that at TiO_2/$MAPbI_3$ (Fig. 1d–f) for both MAI- and PbI_2-terminations (Table 1). For the MAI-termination, the larger binding energy of SnO_2/$MAPbI_3$ interface can be explained with the stronger SSHB at the interface. The binding energy of the interface A/B is calculated by the formula $E_b(A/B) = E(A/B) - E(A) - E(B)$. The binding energy $E_b(SnO_2/MAPbI_3) = E(SnO_2/MAPbI_3) - E(SnO_2) - E(MAPbI_3) = 1.53$ eV/unit-cell which surpasses $E_b(TiO_2/MAPbI_3) = E(TiO_2/MAPbI_3) - E(TiO_2)$

$-E(MAPbI_3) = 1.26$ eV/unit-cell indicates the high stability of $SnO_2/MAPbI_3$ interface (Table 1). The SSHB distance between hydrogen and oxygen atoms at the interface is shorter at the $SnO_2/MAPbI_3$ interface (d(O ··· HN) = 1.54 Å) than at the $TiO_2/MAPbI_3$ interface (d(O ··· HN) = 1.60 Å). Accordingly, the interaction energy of the SSHB, defined as the energy difference between the structure with and without HB between MA and interfacial O at $SnO_2/MAPbI_3$ ($\Delta E = 0.52$ eV/unit-cell) is almost twice stronger than that at $TiO_2/MAPbI_3$ ($\Delta E = 0.27$ eV/unit-cell). The SSHB stabilizes the oxygen dangling bond and enhances the binding energy of interface. For the PbI_2-termination, $E_b(SnO_2/MAPbI_3)$ is 3.00 eV/unit-cell, much stronger than $E_b(TiO_2/MAPbI_3) = 2.40$ eV/unit-cell.

At the PBE-SOC-TS level (Supplementary Figs. 5, 6 and Supplementary Table 2), we note that the band gaps of materials are severely underestimated, resulting in misleading band alignments. For example, at the MAI-terminated $SnO_2/MAPbI_3$ interface with the SSHB (Supplementary Fig. 3c), the CBM of Sn is much lower than the CBM of Pb, indicating a significant open circuit voltage loss of the device. Also, the charge transfer cannot be described accurately within the PBE-SOC-TS level, which results in a fictitious vacuum level shift because of wrong band alignments. Because we need to use the same level of theory to compare two interfaces, we investigated the band gap errors under various DFT functionals (PBE, PBE0, and HSE06) and GW approximation (Supplementary Tables 2, 3, and Methods). We find that the PBE0-SOC-TS shows the lowest average band gap error for the $SnO_2(TiO_2)/MAPbI_3$ interface system.

Table 1. Binding energy (BE), SSHB distance (d(O ··· HN)), and interaction energy (ΔE) of the SSHB in the (a) $SnO_2/MAPbI_3$ and (b) $TiO_2/MAPbI_3$ interfaces. The unit of d(O ··· HN) is given in Å and that of ΔE and BE is given in eV/unit-cell.

a			
Termination/MA orientation	d(O ··· HN)	ΔE	BE
MAI-/[111]	1.54 (SSHB)	0.52	1.53
MAI-/[011]	–	–	0.87
PbI_2-/[001]	–	–	3.00
b			
Termination/MA orientation	d(O ··· HN)	ΔE	BE
MAI-/[111]	1.60 (SSHB)	0.27	1.26
MAI-/[011]	–	–	0.96
MAI-/[001]	–	–	2.40

Quarti et al. showed that the band alignment is significantly influenced by the surface termination type[30]. We find that the band alignment mechanisms are related to the dipole polarization and orbital hybridization[31–34] at MAI-termination and PbI_2-termination, respectively. In order to analyze the band alignment of $SnO_2/MAPbI_3$ and $TiO_2/MAPbI_3$ at each termination, we plot the partial density of states (PDOS) of the $SnO_2/MAPbI_3$ and $TiO_2/MAPbI_3$ interfaces at MAI-termination and PbI_2-termination (Fig. 2). Although the contribution of interfacial atoms is significant for the electron extraction, we included whole atoms in the PDOS diagram, because atoms at bulk also contribute to the VB and CB edges, which is verified by the layer resolved DOS (Supplementary Figs. 7 and 8)[35].

At the MAI-termination, the energy shift is governed by the MA dipolar polarization via the SSHB at the interface, largely affecting the band alignment. The interfacial CBM of SnO_2 is slightly lower (by 0.23 eV) than that of $MAPbI_3$ when the interfacial SSHB exists (Fig. 2a and Supplementary Fig. 9a). Without the SSHB, the band alignment of CBMs becomes unfavorable, as the interfacial CBM of SnO_2 is 0.65 eV higher than that of $MAPbI_3$ (Fig. 2b and Supplementary Fig. 9b), indicating a crucial role of the SSHB for CBM energy shift at the interface. On the contrary, the CBM of TiO_2

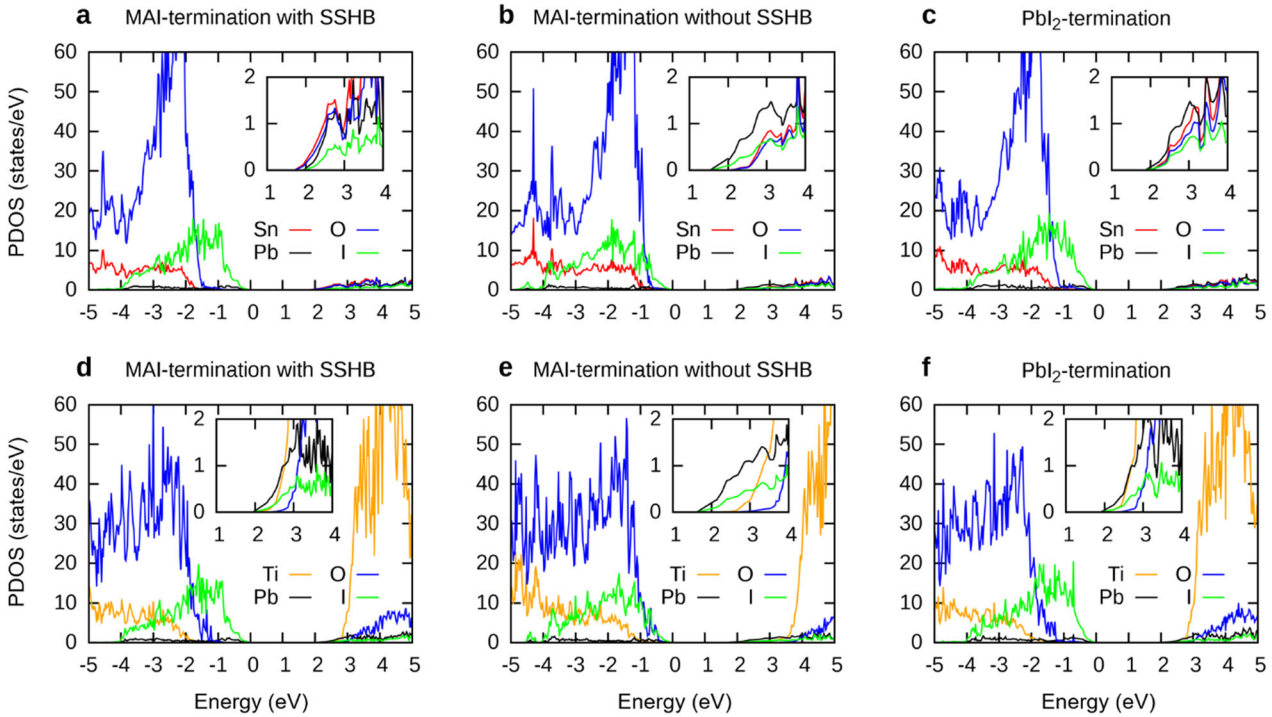

Fig. 2 Partial density of states (PDOS) of $SnO_2/MAPbI_3$ and $TiO_2/MAPbI_3$ interfaces at the PBE0-SOC-TS level. $SnO_2/MAPbI_3$ interface: **a** MAI-termination with the SSHB, **b** MAI-termination without the SSHB, and **c** PbI_2-termination. $TiO_2/MAPbI_3$ interface: **d** MAI-termination with the SSHB, **e** MAI-termination without the SSHB, and **f** PbI_2-termination. The fermi level is set to 0 eV. The $SnO_2/MAPbI_3$ has favorable band alignments for all MA orientations and terminations [Sn (red), Ti (orange), Pb (black), O (blue), and I (green)].

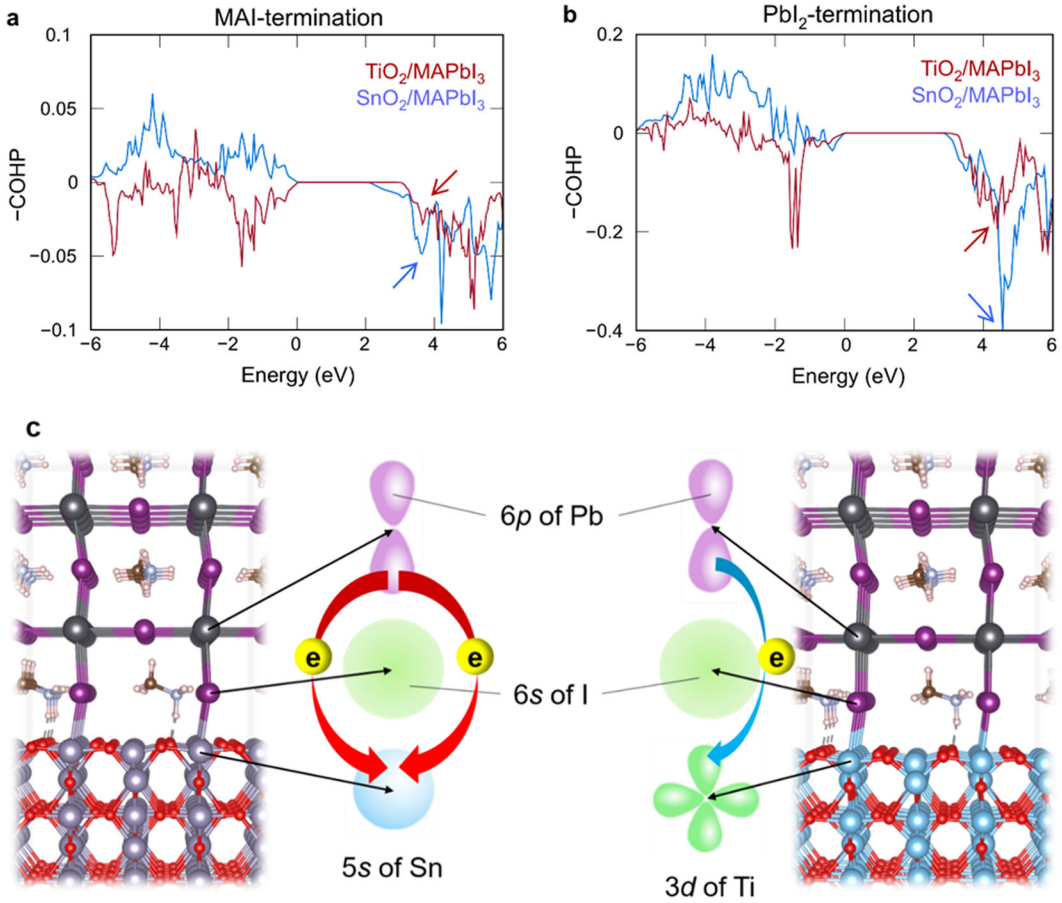

Fig. 3 Averaged crystal orbital Hamiltonian population analysis of interfacial atomic pairs of TiO_2/$MAPbI_3$ (red) and SnO_2/$MAPbI_3$ (blue). **a** MAI-terminated and **b** PbI_2-terminated interfaces at the PBE0-TS level. Both in **a** MAI-termination and **b** PbI_2-terminations, the off-diagonal elements of COHP of SnO_2/$MAPbI_3$ are almost twice of TiO_2/$MAPbI_3$. The larger orbital hybridizations in SnO_2/$MAPbI_3$ at both terminations indicate the superior electron injection to the TiO_2/$MAPbI_3$ interface. **c** Schematic illustration which shows better orbital hybridization between Sn and Pb atoms than Ti and Pb atoms. Left and right geometry indicates MAI-terminated SnO_2/$MAPbI_3$ and TiO_2/$MAPbI_3$, respectively. The larger orbital hybridizations in SnO_2/$MAPbI_3$ at both terminations indicate the superior electron injection to the SnO_2/$MAPbI_3$ interface.

at the interface is always unfavorable regardless of the SSHB (Figs. 2d, e and 9d, e). The CBM of TiO_2 is 0.37 eV (Fig. 2d and Supplementary Fig. 9d) and 1.00 eV (Fig. 2e and Supplementary Fig. 9e) higher than that of $MAPbI_3$. At the PbI_2-termination, SnO_2/$MAPbI_3$ shows 0.17 eV of CBM misalignment (Fig. 2c and Supplementary Fig. 9c). However, such a small misalignment still allows the electron extraction[11,21]. The CBM misalignment at the TiO_2/$MAPbI_3$ interface (Fig. 2f and Supplementary Fig. 9f) is 0.33 eV, which is approximately twice higher than that of the SnO_2/$MAPbI_3$. However, we emphasize that this large misalignment of the TiO_2/$MAPbI_3$ reported here is exaggerated at the PBE0-SOC-TS level. Also, when increasing the number of $MAPbI_3$ layers in the SnO_2/$MAPbI_3$ interface at MAI-termination with SSHB (Supplementary Figs. 10, 11, and Supplementary Table 4) at the PBE-TS level of theory, the band gap of $MAPbI_3$ and the conduction band offset (CBO) are not well converged at three layers of $MAPbI_3$, because of the quantum confinement effect. The band gap of $MAPbI_3$ with 3 layers is overestimated as 1.83 eV compared with the converged band gap of 1.63 eV (6 or more layers of $MAPbI_3$). The CBO of the interface with three $MAPbI_3$ layers is also overestimated as −1.03 eV compared with the converged CBO (−0.68 eV) of the interface with nine $MAPbI_3$ layers or more. The minus sign indicates that the CBM of SnO_2 is lower than that of $MAPbI_3$. Therefore, we note that at least nine layers of $MAPbI_3$ is required for eliminating the quantum confinement effect of the interface. However, the PBE0 + SOC + TS calculations of the interfaces with nine $MAPbI_3$ layers with a huge vacuum (~40 Å) are computationally too demanding even for the-state-of-the-art supercomputers. Therefore, our calculation result focuses on qualitative comparison of the CBO between two interfaces at both terminations.

Also, at PbI_2-termination, the orbital hybridizations of interfacial atoms are significant that the CBM has both Pb ($MAPbI_3$) and Sn (SnO_2) orbital characters (Figs. 2c, f and Supplementary Fig. 12), as Sn and Pb atom makes very similar behavior near the CBM, which contributes to highly efficient electron extraction (Fig. 2c and Supplementary Fig. 12). This large orbital hybridization is manifested in the bonding population analysis based on crystal orbital Hamiltonian population (COHP) (Fig. 3b), which will be elaborated later.

The band gap of bulk SnO_2 and (001) surface has a significant difference (Supplementary Table 5). The calculated band gap (at PBE0-SOC-TS level) of the (001) surface of SnO_2 is 2.92 eV which is much lower than that of bulk SnO_2 (3.58 eV). In contrast, the calculated band gap (at PBE0-SOC-TS level) of the (001) surface of TiO_2 is 3.96 eV which is similar with that of bulk TiO_2 (4.09 eV). This is because of the multivalent property of Sn atom. The surface Sn atoms are reduced from Sn^{4+} to Sn^{2+}, resulting in SnO-like environment at the surface. This reduction makes the Sn-5*s* state filled with electrons near the valence band edge, which reduces the band gap (Supplementary Fig. 13)[36,37]. Thus, a band gap of 2.68 eV (2.65 eV) for SnO_2 (in Supplementary Fig. 9a, c) is not so

much underestimated as that of the (001) surface of SnO_2 (2.92 eV).

The band gap difference between $MAPbI_3$ for MAI-termination with the SSHB (1.95 eV, Supplementary Fig. 9a) and without the SSHB (1.55 eV, Supplementary Fig. 9b) is explained by the presence of the SSHB that significantly affects the band alignments of MAI-terminated interface. The SSHB (between interfacial O of SnO_2 and H of MA) stabilizes the dangling bond of interfacial O of SnO_2, which in turn lowers the CBM of SnO_2. While this interfacial SSHB stabilizes SnO_2, it destabilizes $MAPbI_3$, even though the interface is stabilized overall. The interfacial $MAPbI_3$ has three pairs of hydrogen bonding between I and H of MA. However, these hydrogen bonds inside $MAPbI_3$ are broken in the favor of the SSHB between O of SnO_2 and H of MA. And, this enhances the CBM level of $MAPbI_3$ and increases the band gap (Supplementary Table 6)[38].

The COHP elements at the $SnO_2(TiO_2)$/MAI-terminated $MAPbI_3$ and $SnO_2(TiO_2)/PbI_2$-terminated $MAPbI_3$ interfaces show that the interfacial atom-pairs form dominant antibonding states at both interfaces at the conduction bands (Fig. 3). The off-diagonal elements of COHP spanned by local orbital pairs can provide the covalent contributions (or orbital hybridization) of the bonds and in turn the carrier injections between interfacial atoms. As mentioned, the hybridization is an order of magnitude larger at the PbI_2-termination than the MAI-termination (Figs. 3a, b). This affirms that the orbital hybridization is a dominant mechanism for the band alignment in the PbI_2-termination. Though the hybridization at the MAI-termination is weaker than at the PbI_2-termination, we observe a trend where the off-diagonal COHP elements of conduction bands of $SnO_2/MAPbI_3$ interfacial atoms are larger than those of $TiO_2/MAPbI_3$ by averaging 14 atom-pairs within 2.0–9.0 Å (Fig. 3a). In the PbI_2-terminated $MAPbI_3$ interface, the COHP elements of the conduction bands at $SnO_2/MAPbI_3$ interface are twice larger than those of $TiO_2/MAPbI_3$ interface by averaging 19 atom-pairs within 2.0–5.0 Å. The result clearly indicates the larger orbital hybridization of interfacial atoms and larger electron carrier injection at the $SnO_2/MAPbI_3$ interface (Fig. 3b). The CBMs of SnO_2, TiO_2, and $MAPbI_3$ are mostly composed of Sn-5*s*, Ti-3*d*, and Pb-6*p*, respectively. Thus, the CBM orbital hybridizations occur between Sn-5*s* and Pb-6*p* orbitals at the $SnO_2/MAPbI_3$ interface and between Ti-3*d* and Pb-6*p* at the $TiO_2/MAPbI_3$ interface. This large orbital hybridization could be also verified by the atomic orbital PDOS (Supplementary Fig. 12) in that behavior of Sn-5*s* orbital and Pb-6*p* orbital at the CBM is similar. In general, *d*-orbitals do not strongly hybridize with *s*- or *p*-orbital and the COHP results show that the orbital hybridizations in the $SnO_2/MAPbI_3$ interface are larger than in the $TiO_2/MAPbI_3$ interface (Fig. 3c and Supplementary Fig. 14). Since the orbital hybridization is directly related to the carrier injection at the interface, this can qualitatively explain the reason for the superior carrier injection in $SnO_2/MAPbI_3$ interface which contributes to the high efficiency of PSCs.

Defects are one of the main setbacks for an efficient photovoltaic device, which generate shallow donor/acceptor levels and deep recombination centers around the gap[39,40]. The defect in the ETL hampers the performance of PSC devices because of generation of trap states. Although, defects in the LHP only generates the shallow defect levels close to the band edges which does not damage the electron extraction from LHP to ETL[41], Azpiroz et al. showed that defect migration can hamper the electron extraction at the interface which contributes to the hysteresis of PSC devices[42].

In this work, we mainly focus on how defect states in ETL affect the $SnO_2/MAPbI_3$ and $TiO_2/MAPbI_3$ interface. We study the neutral oxygen vacancy V_o^0 and the Sn(Ti) interstitial $Sn_i^0(Ti_i^0)$ at the surface or interface, which are known to be dominant defects in rutile SnO_2[43,44] and TiO_2[45,46] by employing the supercell layers of SnO_2/TiO_2 (Supplementary Figs. 15 and 16). In pristine TiO_2, both V_o^0 and Ti_i^0 generate deep levels below the CBM (Supplementary Fig. 16e, f), which is consistent with bulk TiO_2[47–49]. For pristine SnO_2, the V_o^0 (bridging) and Sn_i^0 levels are different in the surface and the bulk. For the bulk SnO_2, the V_o^0 creates a shallow level below the CBM in the bulk[37,50]. We find that the interfacial bridging V_o^0 defect forms a SnO-like defect states near the VBM in SnO_2 surface (Supplementary Fig. 16b) by a strong 5*s*–5*p* rehybridization, which is consistent with the previous experiment[51]. We confirm this hypothesis by observing a significant reduction of $Sn^{4+} \rightarrow Sn^{2+}$ from the Bader charge analysis (Supplementary Tables 7 and 8)[52]. For both MAI- and PbI_2-termination, the charge difference of Sn2 atom is the most significant among tin atoms near the V_o^0 (Sn1–Sn4), indicating that charge is localized on Sn2 atom due to V_o^0. Since both surface tin and (Sn2) oxygen have threefold coordination, their charge should be equal with opposite sign. From this, we can confirm the surface is reduced to SnO composition ($Sn^{2+}O^{2-}$), which means the charge of surface tin atom near V_o^0 is reduced from Sn^{4+} to Sn^{2+}. This reduction makes the Sn-5*s* state filled with electrons and results in strong 5*s*–5*p* rehybridization. This unique interfacial defect property, derived from the multi-valency of Sn, creates a favorable electronic environment for the electron transfer between $MAPbI_3$ and SnO_2. While Sn_i^0 forms a shallow level below the CBM (Supplementary Fig. 16c) at SnO_2 surface, bulk Sn_i^0 is a shallow donor inside the CBM in bulk SnO_2[53].

The interfacial V_o^0 at $SnO_2/MAPbI_3$ interface shows the consistent defect states near VBM for MAI- (Fig. 4a) and PbI_2-terminations (Fig. 4c). The band structure of these configurations (Fig. 4a, c) are also calculated (Supplementary Fig. 17a, b), indicating that the occupied 5*s* state of Sn at the surface lies slightly above the top of the valence band. This state does not show any flat dispersion, indicating that this state is due to the multivalence of Sn. Therefore, these SnO-like defect states near the VBM in the $SnO_2/MAPbI_3$ interface (Fig. 4a, c and Supplementary Fig. 17) does not affect the electron extraction process at the CBM. The interfacial Sn_i^0 generates a shallow level near VBM at both MAI- and PbI_2-termination (Fig. 4b, d). On the contrary, the interfacial V_o^0 and Ti_i^0 of TiO_2 create the Ti mid-gap deep level trap states at the MAI- and PbI_2-terminated $TiO_2/MAPbI_3$ interfaces (Fig. 4–h). Therefore, the $SnO_2/MAPbI_3$ interface has the superior defect tolerance to the $TiO_2/MAPbI_3$ interface at both terminations for all dominant defect types.

In summary, we studied the theoretical origin of high electron extraction of SnO_2 ETL for PSCs at the PBE0-SOC-TS level by comparing the $SnO_2/MAPbI_3$ and $TiO_2/MAPbI_3$ interfaces. We calculated the binding energy, band alignment, carrier injection, and the interfacial defect levels at various terminations with different MA directions. We unveil crucial distinction of the conduction band electron transfer mechanisms at the MAI-termination (dipole polarization) and the PbI_2-termination (orbital hybridization) in the $SnO_2(TiO_2)/MAPbI_3$ interface. We explicitly showed that SnO_2 exhibits favorable band alignments to $MAPbI_3$ at both MAI- and PbI_2- terminations over conventional TiO_2 ETL. The carrier injection of the $SnO_2/MAPbI_3$ is larger than that of the $TiO_2/MAPbI_3$ because of strong Sn-5*s* and Pb-5*p*/I-6*s* orbital hybridizations. Also, the interfacial V_o^0 and Sn_i^0 defect levels in SnO_2 do not form deep recombination centers unlike TiO_2 interface. Given that one of the crucial parts of PSC device is ETL, this understanding of electron transfer mechanism in the $SnO_2/MAPbI_3$ interface can pave a way to design better ETL materials for PSCs.

METHODS

We performed the noncollinear density functional theory (DFT) calculations with the hybrid PBE0 functional[54] including TS dispersion correction[55] using Vienna Ab initio Simulation Package[56] with dipole corrections. This is because the PBE0 functional can describe the band alignment of our system very well. In order to choose a suitable exchange-correlations, we performed band gap calculation for bulk SnO_2, TiO_2, and $MAPbI_3$ with different exchange-

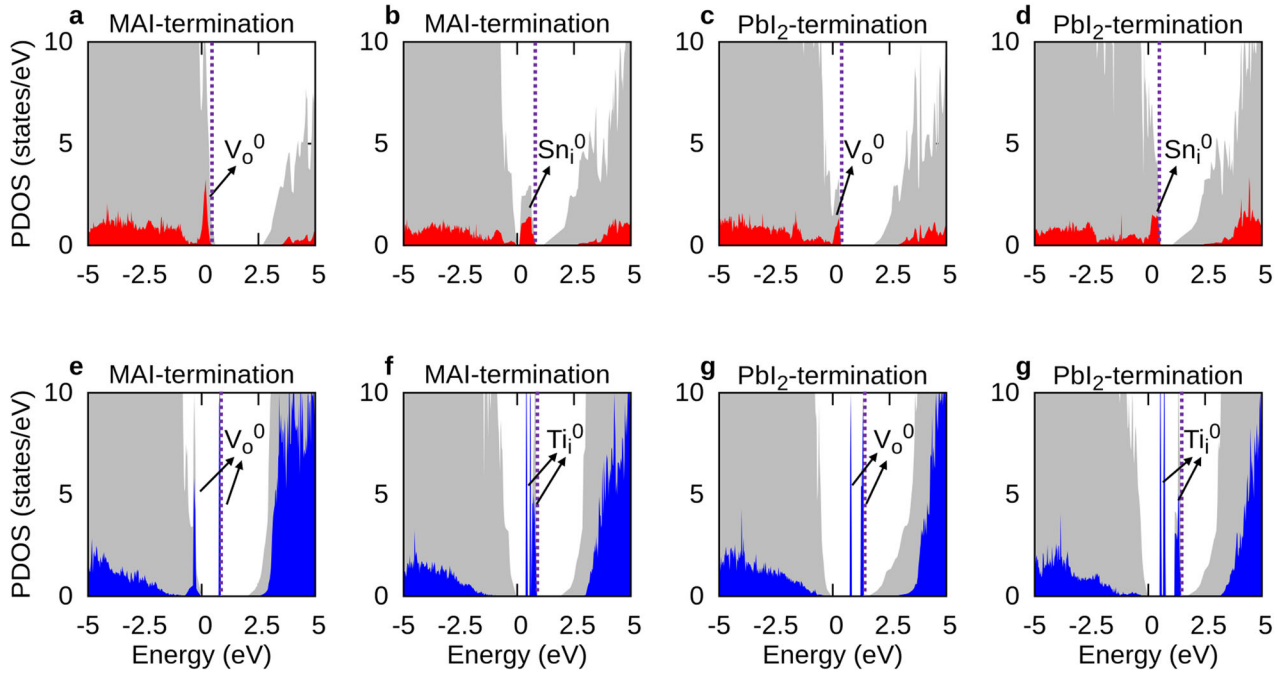

Fig. 4 Partial density of states (PDOS) of SnO_2/$MAPbI_3$ and TiO_2/$MAPbI_3$ interfaces with defects at the PBE0-SOC-TS level. SnO_2/$MAPbI_3$ interface: MAI-termination with **a** oxygen vacancy (V_o^0) and **b** Sn interstitial defect (Sn_i^0), and PbI_2-termination with **c** V_o^0 and **d** Sn_i^0. TiO_2/$MAPbI_3$ interface: MAI-termination with **e** V_o^0 and **f** Ti interstitial defect (Ti_i^0), and PbI_2-termination with **g** V_o^0 and **h** Ti_i^0. The zero of energy represents the top of valence band. The purple dashed line indicates the Fermi level. The SnO_2/$MAPbI_3$ interface shows defect-tolerance for dominant type of defects [Sn atoms near the defect (red), Ti atoms near the defect (blue), and the total DOS (gray)].

correlations, such as PBE, PBE0, and HSE06, including spin–orbit coupling (Supplementary Table 2). For SnO_2, the PBE0-SOC-TS gives the most similar band gap to experiment, whereas the HSE06-SOC-TS gives the most similar band gap to experiment for TiO_2. For MAPbI3, both the PBE and the PBE0-SOC-TS give similar band gaps to experiment. We noted that regardless of exchange-correlation, theoretical band gap is larger in TiO_2, whereas experimental band gap is larger in SnO_2. The same trend is also noted in the GW calculation of bulk SnO_2 and TiO_2 (Supplementary Table 3). Therefore, instead of choosing different exchange-correlation for SnO_2/$MAPbI_3$ and TiO_2/$MAPbI_3$ interface, we selected only one potential for the whole interface calculations which can minimize the average band gap error. Since the PBE0-SOC-TS gives the minimum band gap error compared with the experimental band gap, we choose the PBE0-SOC-TS exchange-correlation. In order to check surface properties, we also calculated the band gap of (001) surface of SnO_2 and TiO_2 at the PBE0-SOC-TS level (Supplementary Table 4). We used PAW pseudopotentials of Ti($3s^2 3p^6 3d^2 4s^2$), Sn($4d^{10} 5s^2 5p^2$), O($2s^2 2p^4$), Pb($5d^{10} 6s^2 6p^2$), and I($5s^2 5p^5$). We employed ***Γ***-centered ($4 \times 4 \times 1$) *k*-mesh for sampling the Brillouin zone and 560 eV energy cutoff for the planewave basis. Structural geometry optimization was performed with energy convergence and force convergence of 10^{-6} eV and 0.02 eV/Å, respectively (Fig. 1 and Supplementary Table 9). The COHP analysis was done using LOBSTER v.3.1.0[57]. COHP is a theoretical bond-detecting tool for solids, which partitions the band-structure energy into orbital–pair interactions.

In order to obtain the quantitative band alignments (Supplementary Fig. 9), we extracted the band alignment from the PDOS of bulk-like regions of the respective layers (L3 for SnO_2 (TiO_2) and L2 for $MAPbI_3$ in Supplementary Figs. 7 and 8). Also, in order to show the PDOS method is reliable, we calculated the CBO for MAI-termination with SSHB and PbI_2-termination of SnO_2/$MAPbI_3$ interface (Supplementary Fig. 18) by using an alternative method called Hartree potential alignment. In order to obtain the CBO of the interface A/B by using Hartree potential alignment, we need the Hartree potentials (VH) of the interface (A/B) and its corresponding A and B structure with the lattice parameter of the interface (or constrained bulk systems from the geometry of the interface). Then, the Hartree potentials of A and B are vertically shifted to be overlapped with the Hartree potential of the interface (A/B), where A and B are SnO_2 and $MAPbI_3$ in our system, respectively. Here, we obtain the shifts of the Hartree potential $VH_{A/B\text{-}A}$ (energy shift between the interface A/B and A) and $VH_{A/B\text{-}B}$ (energy shift between the interface A/B and B) (Supplementary Fig. 18a, b). The CBO is calculated by $CBO = (CB_B + VH_{A/B\text{-}B}) - (CB_A + VH_{A/B\text{-}A}) = (CB_B - CB_A) + (VH_{A/B\text{-}B} - VH_{A/B\text{-}A})$, where CB_A and CB_B are the CBM of the corresponding A and B structure of the interface A/B. Both the PDOS method and the Hartree potential alignment can be used to obtain band alignments, assuming the interface is thick enough to have bulk-like properties and dense *k*-points are used[35].

For MAI-termination with SSHB of SnO_2/$MAPbI_3$ interface, we obtain the CBO of −0.23 eV from the PDOS method (Supplementary Fig. 9a), as compared with the CBO of −0.29 eV from the Hartree potential alignment (Supplementary Fig. 18c). For PbI_2-termination of SnO_2/$MAPbI_3$ interface, similarly, we obtain the CBO of +0.17 eV from the PDOS method (Supplementary Fig. 9c), as compared with the CBO of +0.11 eV from the Hartree potential alignment (Supplementary Fig. 18d). The plus/minus sign of the CBO indicates that the CBM of SnO_2 is higher/lower than that of $MAPbI_3$. For both terminations, the CBO difference between the PDOS method and the Hartree potential alignment is within 60 meV, indicating that the results of our PDOS method are reliable[58]. Therefore, we used this PDOS method for the analysis of whole systems.

DATA AVAILABILITY

The data that support the findings of this study are available from the corresponding author upon reasonable request.

CODE AVAILABILITY

All codes used to calculate the presented results are available from the corresponding author upon reasonable request.

Received: 14 October 2019; Accepted: 22 June 2020;
Published online: 16 July 2020

REFERENCES

1. Javaid, S., Myung, C. W., Yun, J., Lee, G. & Kim, K. S. Organic cation steered interfacial electron transfer within organic-inorganic perovskite solar cells. *J. Mater. Chem. A.* **6**, 4305 (2018).

2. Myung, C. W., Javaid, S., Kim, K. S. & Lee, G. Rashba-Dresselhaus effect in inorganic/organic lead iodide perovskite interfaces. *ACS Energy Lett.* **3**, 1294 (2018).
3. De Angelis, F. et al. Trends in perovskite solar cells and optoelectronics: status of research and applications from the PSCO conference. *ACS Energy Lett.* **2**, 857 (2017).
4. Ko, K. C., Bromley, S. T., Lee, J. Y. & Illas, F. Size-dependent level alignment between rutile and anatase TiO_2 nanoparticles: implications for photocatalysis. *J. Phys. Chem. Lett.* **8**, 5593 (2017).
5. Jeon, J. et al. Polymorphic phase control mechanism of organic-inorganic hybrid perovskite engineered by dual-site alloying. *J. Phys. Chem. C.* **121**, 9508 (2017).
6. Motta, C. et al. Revealing the role of organic cations in hybrid halide perovskite $CH_3NH_3PbI_3$. *Nat. Commun.* **6**, 7026 (2015).
7. Zheng, F., Tan, L. Z., Liu, S. & Rappe, A. M. Rashba spin−orbit coupling enhanced carrier lifetime in $CH_3NH_3PbI_3$. *Nano Lett.* **15**, 7794 (2015).
8. Zhou, H. et al. Interface engineering of highly efficient perovskite solar cells. *Science* **345**, 542 (2014).
9. Yang, G., Tao, H., Qin, P., Ke, W. & Fang, G. Recent progress in electron transport layers for efficient perovskite solar cells. *J. Mater. Chem. A* **4**, 3970 (2016).
10. Mosconi, E. et al. Enhanced TiO_2/$MAPbI_3$ electronic coupling by interface modification with PbI_2. *Chem. Mater.* **28**, 3612 (2016).
11. Dong, Q. et al. Improved SnO_2 electron transport layers solution-deposited at near room temperature for rigid or flexible perovskite solar cells with high efficiencies. *Adv. Energy Mater.* **9**, 1900834 (2019).
12. Roose, B. et al. Mesoporous SnO_2 electron selective contact enables UV-stable perovskite solar cells. *Nano Energy* **30**, 517 (2016).
13. Leijtens, T. et al. Overcoming ultraviolet light instability of sensitized TiO_2 with meso-superstructured organometal Tri-halide perovskite solar cells. *Nat. Commun.* **4**, 1 (2013).
14. Kim, H. S., Im, S. H. & Park, N. G. Organolead halide perovskite: new horizons in solar cell research. *J. Phys. Chem. C.* **118**, 5615 (2014).
15. Yella, A., Heiniger, L. P., Gao, P., Nazeeruddin, M. K. & Grätzel, M. Nanocrystalline rutile electron extraction layer enables low-temperature solution processed perovskite photovoltaics with 13.7% efficiency. *Nano Lett.* **14**, 2591 (2014).
16. Abate, A. et al. Silolothiophene-linked triphenylamines as stable hole transporting materials for high efficiency perovskite solar cells. *Energy Environ. Sci.* **8**, 2946 (2015).
17. Ogomi, Y. et al. $CH_3NH_3Sn_xPb_{(1-x)}I_3$ perovskite solar cells covering up to 1060 nm. *J. Phys. Chem. Lett.* **5**, 1004 (2014).
18. Dong, Q., Shi, Y., Zhang, C., Wu, Y. & Wang, L. Energetically favored formation of SnO_2 nanocrystals as electron transfer layer in perovskite solar cells with high efficiency exceeding 19%. *Nano Energy* **40**, 336 (2017).
19. Myung, C. W., Lee, G. & Kim, K. S. La-doped $BaSnO_3$ electron transport layer for perovskite solar cells. *J. Mater. Chem. A* **6**, 23071 (2018).
20. Liu, D. & Kelly, T. L. Perovskite solar cells with a planar heterojunction structure prepared using room-temperature solution processing techniques. *Nat. Photonics* **8**, 133 (2014).
21. Correa Baena, J. P. et al. Highly efficient planar perovskite solar cells through band alignment engineering. *Energy Environ. Sci.* **8**, 2928 (2015).
22. Batzill, M. & Diebold, U. The surface and materials science of tin oxide. *Prog. Surf. Sci.* **79**, 47 (2005).
23. Amtout, A. & Leonelli, R. Optical properties of rutile near its fundamental band gap. *Phys. Rev. B.* **51**, 6842 (1995).
24. Yang, G. et al. Effective carrier-concentration tuning of SnO_2 quantum dot electron-selective layers for high-performance planar perovskite solar cells. *Adv. Mater.* **30**, 1 (2018).
25. Liu, Q. et al. Enhanced stability of perovskite solar cells with low-temperature hydrothermally grown SnO_2 electron transport layers. *Adv. Funct. Mater.* **26**, 6069 (2016).
26. Tiwana, P., Docampo, P., Johnston, M. B., Snaith, H. J. & Herz, L. M. Electron mobility and injection dynamics in mesoporous ZnO, SnO_2, and TiO_2 films used in dye-sensitized solar cells. *ACS Nano* **5**, 5158 (2011).
27. Wali, Q., Fakharuddin, A. & Jose, R. Tin oxide as a photoanode for dye-sensitised solar cells: current progress and future challenges. *J. Power Sources* **293**, 1039 (2015).
28. Xiong, L. et al. Fully high-temperature-processed SnO_2 as blocking layer and scaffold for efficient, stable, and hysteresis-free mesoporous perovskite solar cells. *Adv. Funct. Mater.* **28**, 1 (2018).
29. Song, J. et al. Low-temperature SnO_2-based electron selective contact for efficient and stable perovskite solar cells. *J. Mater. Chem. A* **3**, 10837 (2015).
30. Quarti, C., De Angelis, F. & Beljonne, D. Influence of surface termination on the energy level alignment at the $CH_3NH_3PbI_3$ perovskite/C60 interface. *Chem. Mater.* **29**, 958 (2017).
31. Wilson, N. R. et al. Determination of band offsets, hybridization, and exciton binding in 2D semiconductor heterostructures. *Sci. Adv.* **3**, e1601832 (2017).
32. Li, L., Li, P., Lu, N., Dai, J. & Zeng, X. C. Simulation evidence of hexagonal-to-tetragonal ZnSe structure transition: a monolayer material with a wide-range tunable direct bandgap. *Adv. Sci.* **2**, 1 (2015).
33. Wang, H., Wei, W., Li, F., Huang, B. & Dai, Y. Step-like band alignment and stacking-dependent band splitting in trilayer TMD heterostructures. *Phys. Chem. Chem. Phys.* **20**, 25000 (2018).
34. Dou, M. & Persson, C. Comparative study of rutile and anatase SnO_2 and TiO_2: band-edge structures, dielectric functions, and polaron effects. *J. Appl. Phys.* **113**, 083703 (2013).
35. Traore, B. et al. Importance of vacancies and doping in the hole-transporting nickel oxide interface with halide perovskites. *ACS Appl. Mater. Interfaces* **12**, 6633 (2020).
36. Mäki-Jaskari, M. A. & Rantala, T. T. Band structure and optical parameters of the SnO_2(110) surface. *Phys. Rev. B.* **64**, 1 (2001).
37. Batzill, M. et al. Gas-phase-dependent properties of SnO_2 (110), (100), and (101) single-crystal surfaces: structure, composition, and electronic properties. *Phys. Rev. B.* **72**, 1 (2005).
38. Lee, J. H., Lee, J. H., Kong, E. H. & Jang, H. M. The nature of hydrogen-bonding interaction in the prototypic hybrid halide perovskite, tetragonal $CH_3NH_3PbI_3$. *Sci. Rep.* **6**, 1 (2016).
39. Li, L. & Carter, E. A. Defect-mediated charge-carrier trapping and nonradiative recombination in WSe2 monolayers. *J. Am. Chem. Soc.* **141**, 10451 (2019).
40. Haruyama, J., Sodeyama, K., Hamada, I., Han, L. & Tateyama, Y. First-principles study of electron injection and defects at the TiO_2/$CH_3NH_3PbI_3$ interface of perovskite solar cells. *J. Phys. Chem. Lett.* **8**, 5840 (2017).
41. Yin, W. J., Shi, T. & Yan, Y. Unusual defect physics in $CH_3NH_3PbI_3$ perovskite solar cell absorber. *Appl. Phys. Lett.* **104**, 063903 (2014).
42. Azpiroz, J. M., Mosconi, E., Bisquert, J. & De Angelis, F. Defect migration in methyl ammonium lead iodide and its role in perovskite solar cell operation. *Energy Environ. Sci.* **8**, 2118 (2015).
43. Kar, A., Kundu, S. & Patra, A. Surface defect-related luminescence properties of SnO_2 nanorods and nanoparticles. *J. Phys. Chem. C.* **115**, 118 (2011).
44. Shi, S., Gao, D., Xu, Q., Yang, Z. & Xue, D. Singly-charged oxygen vacancy-induced ferromagnetism in mechanically milled SnO_2 powders. *RSC Adv.* **4**, 45467 (2014).
45. Pan, X., Yang, M. Q., Fu, X., Zhang, N. & Xu, Y. J. Defective TiO_2 with oxygen vacancies: synthesis, properties and photocatalytic applications. *Nanoscale* **5**, 3601 (2013).
46. Wendt, S. et al. The role of interstitial sites in the band gap of titania. *Science* **320**, 1755 (2008).
47. Cho, E. et al. First-principles study of point defects in rutile TiO_{2-X}. *Phys. Rev. B.* **73**, 2 (2006).
48. Mulheran, P. A. et al. Surface and interstitial Ti diffusion at the rutile TiO_2 (110) surface. *Phys. Chem. Chem. Phys.* **12**, 9763 (2010).
49. Lee, H. Y., Clark, S. J. & Robertson, J. Calculation of point defects in rutile TiO_2 by the screened-exchange hybrid functional. *Phys. Rev. B.* **86**, 1 (2012).
50. Godinho, K. G., Walsh, A. & Watson, G. W. Energetic and electronic structure analysis of intrinsic defects in SnO_2. *J. Phys. Chem. C.* **113**, 439 (2009).
51. Kılıç, Ç. & Zunger, A. Origins of coexistence of conductivity and transparency in SnO_2. *Phys. Rev. Lett.* **88**, 955011 (2002).
52. Tang, W., Sanville, E. & Henkelman, G. A grid-based bader analysis algorithm without lattice bias. *J. Phys. Condens. Matter* **21**, 084204 (2009).
53. Cox, F., Fryberger, T. B. & Semancik, S. Oxygen vacancies and defect electronic states on the SnO_2 (110)-1x1 surface. *Phys. Rev. B.* **38**, 2072 (1988).
54. Perdew, J. P., Burke, K. & Ernzerhof, M. Generalized gradient approximation made simple. *Phys. Rev. Lett.* **77**, 3865 (1996).
55. Tkatchenko, A. & Scheffler, M. Accurate molecular Van Der Waals interactions from ground-state electron density and free-atom reference data. *Phys. Rev. Lett.* **102**, 073005 (2009).
56. Kresse, G. & Furthmuller, J. Efficiency of ab-initio total energy calculations for metals and semiconductors using a plane-wave basis set. *Comput. Mater. Sci.* **6**, 15 (1996).
57. Maintz, S., Deringer, V. L., Tchougréeff, A. L. & Dronskowski, R. LOBSTER: a tool to extract chemical bonding from plane-wave based DFT. *J. Comput. Chem.* **37**, 1030 (2016).
58. Junquera, J., Zimmer, M., Ordejón, P. & Ghosez, P. First-principles calculation of the band offset at BaO/$BaTiO_3$ and SrO/$SrTiO_3$ interfaces. *Phys. Rev. B.* **67**, 155327 (2003).

ACKNOWLEDGEMENTS

This work was supported by NRF (National Honor Scientist Program: 2010-0020414). K.S.K. acknowledges the support from KISTI (KSC-2018-CHA-0057, KSC-2018-CRE-0077, KSC-2019-CRE-0103, KSC-2019-CRE-0253, KSC-2020-CRE-0049). C.W.M.

acknowledges the support from KISTI (KSC-2018-CRE-0071, KSC-2019-CRE-0139, KSC-2019-CRE-0248). J.K. acknowledges the support from KISTI (KSC-2018-CRE-0055, KSC-2019-CRE-0064, KSC-2019-CRE-0244). J.K thanks to Dr. Sung Bum Kang for valuable discussions.

AUTHOR CONTRIBUTIONS

C.W.M. and J.K. conceived the idea and devised the theory. J.K. and C.W.M. performed all calculations. All authors wrote the manuscript. K.S.K. and C.W.M. supervised the project.

COMPETING INTERESTS

The authors declare no competing interests.

ADDITIONAL INFORMATION

Supplementary information is available for this paper at https://doi.org/10.1038/s41524-020-00370-y.

Correspondence and requests for materials should be addressed to K.S.K. or C.W.M.

Reprints and permission information is available at http://www.nature.com/reprints

Publisher's note Springer Nature remains neutral with regard to jurisdictional claims in published maps and institutional affiliations.